Adıyaman University
Journal of Engineering Sciences
Adyü J Eng Sci 2026;13:e260128
Adıyaman Üniversitesi
Mühendislik Bilimleri Dergisi
Adyü Müh Bil Derg 2026;13:e260128
https://doi.org/10.54365/adyumbd.1911181

Research Article / Araştırma Makalesi

Torque and Torque Ripple-Focused Performance Evaluation of Outer-Rotor Synchronous Reluctance Motors with Hybrid Flux-Barrier Rotor Structure

Hibrit Akı Bariyerli Dıştan Rotorlu Senkron Relüktans Motorlarının Tork ve Tork Dalgalanması Odaklı Performans Değerlendirmesi

Şükrü Özdemir [1] *, Mustafa Eker [2]

[1] Artvin Çoruh University, Borçka Acarlar Vocational School, Department of Electricity and Energy, Artvin, Türkiye
[2] Tokat Gaziosmanpaşa University, Faculty of Engineering, Department of Electrical and Electronics Engineering, Tokat, Türkiye

Abstract

In this study, the electromagnetic performance of an Outer-Rotor Synchronous Reluctance Motor (OR-SynRM) is investigated by analyzing different rotor flux barrier geometries. The stator geometry, winding structure, and operating conditions are kept constant, while only the number, geometry, and arrangement of the rotor flux barriers are varied. Based on four fundamental barrier geometries (elliptical, triangular, U1, and U2), hybrid rotor topologies with two and three barriers are developed, resulting in a total of 34 motor designs. The electromagnetic behavior is analyzed using a two-dimensional time-stepping Finite Element Method (FEM) based on Maxwell's equations. During the optimization process, a Multi-Objective Genetic Algorithm (MOGA) is applied, in which average electromagnetic torque and torque ripple are equally weighted. The results show that the number and geometry of the barriers strongly influence magnetic flux distribution, torque production, and torque ripple characteristics. Back Electromotive Force (back-EMF) waveform and harmonic analyses indicate that multi-barrier rotor structures provide a more balanced electromagnetic performance.

Keywords: *OR-SynRM, Hybrid Rotor Flux Barriers, Torque Ripple, MOGA, Induced Voltage Harmonics*

Öz

Bu çalışmada, dıştan rotorlu senkron relüktans motorunun (Outer-Rotor Synchronous Reluctance Motor – OR-SynRM) elektromanyetik performansı farklı rotor akı bariyeri geometrilerinin analiz edilmesi yoluyla incelenmiştir. Stator geometrisi, sargı yapısı ve çalışma koşulları sabit tutulmuş, yalnızca rotor akı bariyerlerinin sayısı, geometrisi ve yerleşimi değiştirilmiştir. Dört temel bariyer geometrisine (eliptik, üçgensel, U1 ve U2) dayanarak iki ve üç bariyerli hibrit rotor topolojileri geliştirilmiş ve toplamda 34 farklı motor tasarımı elde edilmiştir. Elektromanyetik davranış, Maxwell denklemlerine dayalı iki boyutlu zaman adımlı Sonlu Elemanlar Yöntemi (Finite Element Method – FEM) kullanılarak analiz edilmiştir. Optimizasyon sürecinde Çok Amaçlı Genetik Algoritma (Multi-Objective Genetic Algorithm–MOGA) uygulanmış ve ortalama elektromanyetik moment ile moment dalgalanmasına eşit ağırlık verilmiştir. Elde edilen sonuçlar, bariyerlerin sayısı ve geometrisinin manyetik akı dağılımını, moment üretimini ve moment dalgalanması karakteristiklerini güçlü bir şekilde etkilediğini göstermektedir. Zıt elektromotor kuvveti (Back Electromotive Force – back-EMF) dalga formu ve harmonik analizleri, çok bariyerli rotor yapılarının daha dengeli bir elektromanyetik performans sağladığını ortaya koymaktadır.

Anahtar Kelimeler: *OR-SynRM, Hibrit Rotor Akı Bariyerleri, Tork Dalgalanması, Çok Amaçlı Genetik Algoritma (MOGA), İndüklenen Gerilim Harmonikleri*

* Corresponding e-mail (Sorumlu yazar e-posta): sukruozdemir@artvin.edu.tr
Received (Geliş Tarihi):17.03.2026, **Accepted (Kabul Tarihi):** 18.05.2026

1. Introduction

In electric motor design, energy efficiency, high torque density, low maintenance requirements, and cost-effectiveness are key criteria. Synchronous reluctance motors (SynRMs), whose rotors contain neither permanent magnets nor windings, offer advantages such as low rotor losses, high thermal robustness, and a simple mechanical structure. For these reasons, SynRMs have emerged as an alternative solution for industrial drives and variable-speed applications[1,2]. SynRM performance depends largely on rotor magnetic saliency; the saliency ratio (L_d/L_q), which reflects the difference between the d-axis and q-axis inductances, directly affects electromagnetic torque production. Therefore, rotor geometry—particularly the number, shape, and placement of flux barriers in the rotor—plays a critical role in SynRM design[3]. Poorly designed barrier geometries can increase torque ripple and electromagnetic harmonics while raising the average torque[4]. Outer-rotor SynRMs (OR-SynRMs) are particularly advantageous for direct-drive applications requiring high torque at low speed; a larger effective radius enables higher electromagnetic torque at the same current level and can eliminate mechanical gear-reduction components in some systems[5]. This structural advantage explains the growing interest in OR-SynRMs in areas such as electric bicycles, scooters, low-speed industrial drives, and precision positioning systems[6]. Nevertheless, high torque ripple—associated with vibration, acoustic noise, and back-EMF (back electromotive force) harmonics—limits broader adoption by degrading performance, particularly at low speeds[7]. Studies indicate that the primary source of torque ripple is rotor flux-barrier geometry (i.e., the number and shape of the barriers)[8,9]; however, constructing a broad design space extending from basic geometries to hybrid structures and systematically comparing it has remained limited in the literature[10]. It has also been noted that optimization in most studies focuses only on average torque or power factor, while torque ripple and back-EMF harmonic performance are treated as secondary criteria[11].

This study addresses the limited availability of systematic investigations that simultaneously consider different rotor flux-barrier geometries, barrier numbers, and hybrid configurations within a unified framework. While the stator structure and winding parameters are kept constant, only the rotor flux-barrier geometries are varied to ensure a consistent comparison. Four fundamental barrier geometries—triangular, elliptical, U1, and U2—are combined in dual- and triple-barrier arrangements, resulting in 34 distinct rotor configurations. Each design is optimized using a multi-objective genetic algorithm (MOGA) with equal emphasis on average torque and torque ripple, and is evaluated in terms of back-EMF waveform characteristics, harmonic content, and magnetic flux behavior. Accordingly, this study provides a comprehensive and comparative perspective that highlights the role of hybrid barrier design in improving torque stability and electromagnetic performance in OR-SynRMs.

In order to clearly highlight the novelty and contributions of this study, the main contributions can be summarized as follows:

- A comprehensive design space consisting of 34 different rotor configurations is established by combining four fundamental flux barrier geometries (elliptical, triangular, U1, and U2) in both dual- and triple-barrier arrangements.
- A systematic and fair comparison framework is developed by keeping the stator geometry, winding configuration, and operating conditions constant, allowing the direct evaluation of rotor geometry effects on electromagnetic performance.
- A hybrid flux-barrier design approach is proposed, enabling improved control of d-axis flux paths and q-axis reluctance, leading to enhanced torque production and torque ripple characteristics.
- A multi-objective optimization framework based on the MOGA algorithm is implemented, simultaneously considering average torque and torque ripple with equal weighting.
- The electromagnetic performance of all designs is evaluated using time-stepping FEM, including torque, torque ripple, flux distribution, and back-EMF harmonic characteristics.
- A combined analysis of torque production and harmonic behavior is presented, demonstrating that hybrid rotor structures provide a more balanced electromagnetic performance rather than a monotonic improvement.

- The study provides a generalized design methodology for OR-SynRM rotor optimization in low-speed, high-torque applications.

2. Literature Review

In recent years, it has begun to be emphasized in previous studies that OR-SynRMs should be evaluated not only from an electromagnetic perspective but also from a mechanical point of view. In their study conducted on a modular OR-SynRM, Jurca, Inte, and Martis considered electromagnetic and mechanical analyses together and demonstrated that rotor geometry directly affects not only torque production but also mechanical stress, vibration, and structural integrity[12]. This study is important in that it reveals the necessity of integrating mechanical constraints into the design process while targeting high torque density in OR-SynRMs. The evaluation of OR-SynRM in terms of reliability and fault tolerance has also constituted an important line of research in earlier investigations. Bonthu and co-workers investigated the fault-tolerant performance of outer- and inner-rotor Permanent Magnet–Assisted Synchronous Reluctance Motors (PM-assisted SynRMs) through a comparative study and showed that rotor architecture plays a decisive role in electromagnetic behavior under fault conditions [13]. Similarly, the performance of five-phase Outer-Rotor PM-assisted SynRMs in in-wheel applications has been investigated, and it has been reported that the multi-phase structure provides advantages in terms of torque continuity and reliability[14]. These studies indicate that, in outer-rotor machines, not only nominal performance but also behavior under fault conditions should be considered as a design criterion. In the application-oriented literature, the suitability of OR-SynRMs, particularly for scooters and light electric vehicles, has been discussed in detail. Salehinia et al. proposed a systematic design procedure for an OR-SynRM intended for scooter applications and demonstrated that the simultaneous selection of rotor and stator parameters is decisive for average torque, efficiency, and torque ripple[15]. This study shows that OR-SynRMs offer a practical alternative for vehicle applications requiring low speed and high torque. The optimization of rotor geometry is one of the main focal points in the OR-SynRM literature. In the study carried out by Jurca, Inte, and Martis, the optimal rotor design for a novel OR-SynRM was addressed, and it was shown that the number and shape of flux barriers have a direct effect on saliency ratio (L_d/L_q) power factor, and average torque[16]. This study clearly demonstrates that rotor flux barriers should be considered not only numerically but also together with their geometric forms. PM-assisted OR-SynRMs also occupy an important place in existing studies. Moradi CheshmehBeigi and Behroozi examined the effects of rotor geometry on torque production, efficiency, and saturation behavior in detail by jointly addressing analytical design and electromagnetic field analysis for an outer-rotor PM-assisted SynRM[17]. However, it is also emphasized in existing studies that such assisted structures involve disadvantages such as increased cost and demagnetization risk. Studies focusing on more complex machine topologies are also available in existing research. Al-ani presented a multi physics design and analysis approach for double rotor SynRMs demonstrating that thermal and mechanical constraints should be integrated into the design process in addition to electromagnetic performance[18]. Such studies reveal that optimization problems should not be limited solely to electromagnetic objectives. The reduction of torque ripple is one of the most intensively studied topics in the OR-SynRM literature. Bonthu, Tarek, and Choi proposed an optimal torque ripple reduction technique for outer-rotor PM-assisted SynRM and demonstrated that torque ripple can be significantly suppressed through appropriate design of the rotor and auxiliary magnet arrangement[19]. In this context, the performances of rare-earth and non–rare-earth outer-rotor motors under eccentricity faults have been investigated, and the sensitivity of rotor architecture to such faults has been revealed [20]. The sensitivity of rotor geometry to performance is also a critical research area in OR-SynRM design. Hefaz, Afjei, and Ardestani analyzed the effect of rotor geometry on electromagnetic performance in OR-SynRMs using the FEM and demonstrated that small geometric variations can lead to significant changes in torque and torque ripple[21]. Similarly, in the study conducted by Dirba, Lavrinovicha, and Dobriyan, the general design principles of SynRMs were discussed, and the decisive role of rotor geometry on performance was emphasized[22]. Comparisons of the outer-rotor architecture with different machine types are also reported in published studies. Mukherjee and co-workers compared inner and outer-rotor bearingless SynRM and examined the effects of rotor architecture on electromagnetic behavior and application suitability[23]. This study indicates that while the outer rotor structure provides advantages in certain applications, it may also introduce additional challenges in terms of control and design. The effect of winding topology on torque ripple has also been addressed in the OR-SynRM literature. Inte and Jurca investigated torque ripple reduction in an OR-SynRM with concentrated windings and showed that the winding arrangement directly affects ripple components[24]. Similarly, sensitivity analyses focusing on rotor geometry in outer-rotor PM-assisted SynRMs have been conducted, and the effects of geometric parameters on performance have been reported in detail[25]. Finally, in studies comparing permanent magnet and magnet-free versions of OR-SynRM, it has been stated that the use of auxiliary magnets improves average torque and efficiency but introduces additional disadvantages in terms of cost and complexity [26]. These results once again demonstrate how critical rotor flux barrier geometry is in magnet-free OR-SynRMs.

Overall, studies on OR-SynRMs have mainly focused on low-speed applications, torque ripple reduction, rotor geometry sensitivity, and the effects of auxiliary structures. However, it is observed that studies addressing the evolution of flux barrier geometries from basic structures to hybrid structures over a broad design space and within a systematic optimization framework remain limited in available studies. Although mechanical stress, vibration, and structural integrity are important aspects in the design of OR-SynRMs, the present study is deliberately limited to electromagnetic performance analysis, with mechanical evaluations left as a subject for future work. This study aims to fill this gap by evaluating 34 different rotor designs including double and triple barrier arrangements and their hybrid combinations based on four fundamental barrier geometries (triangular, elliptical, U1, and U2) under the same stator structure.

3. Mathematical Modeling and Performance Metrics of the OR-SynRM

In this section, the mathematical framework used to describe the electromagnetic behavior of the OR-SynRM is presented in detail. The provided model covers electromagnetic field theory, the dq-axis machine model, the torque production mechanism, power balance, torque ripple, and back-EMF harmonics. All expressions presented are taken as the basis for interpreting the results obtained from the Finite Element Analyses (FEA) of the motor with 34 different rotor flux barrier geometries investigated in this study. In this work, the stator geometry, winding structure, and operating conditions are kept constant, and only the number and geometry of the rotor flux barriers are varied. Accordingly, the subsequent subsections present the governing electromagnetic field equations, dq-axis relations, torque and ripple metrics, and harmonic definitions that are used consistently to interpret the FEM results for all 34 rotor barrier configurations. Therefore, while many parameters appearing in the mathematical expressions (e.g., winding factor k_w, number of series turns per phase N_s, stator diameter D_s, Root Mean Square (RMS) voltage V_{rms} and RMS current I_{rms}) remain constant, rotor related parameters (L_d, L_q, saturation coefficients, barrier reluctances, etc.) differ among the motors. This approach makes the comparison of the 34 designs under the condition of same stator and different rotor barrier geometries methodologically consistent.

3.1. Electromagnetic Field Fundamental

3.1.1. Maxwell's Equations and Magnetic Field Definition

The electromagnetic field distribution in electrical machines is governed by Maxwell's equations. In differential form, the fundamental Maxwell equations are expressed as follows:

$$\nabla \times \mathrm{H} = \mathrm{J} + \frac{\partial \mathrm{D}}{\partial t} \tag{1}$$

$$\nabla \times \mathrm{E} = -\frac{\partial \mathrm{B}}{\partial t} \tag{2}$$

$$\nabla \cdot \mathrm{B} = 0 \tag{3}$$

$$\mathrm{B} = \mu \mathrm{H} \tag{4}$$

Here, E denotes the electric field intensity, H the magnetic field intensity, B the magnetic flux density, J the current density, D the electric flux density, and μ the magnetic permeability of the material[27-28]. In the analysis of electrical machines, the Magneto–Quasi-Static (MQS) approach is generally employed. In this approach, the displacement current term $\partial \mathrm{D}/\partial \mathrm{t}$ is neglected, and the electromagnetic behavior is primarily modeled through the relationship between the current density J and the magnetic field H [29-30]. In the evaluation of the electromagnetic behavior of electrical machines, quantities such as magnetic flux density, flux lines, electromagnetic torque, and back-EMF are commonly obtained using the FEM based on Maxwell's equations[27,29]. When the rotor barrier geometry is modified, the B distribution is reshaped in the rotor bridges and stator tooth tips: this variation affects magnetic saturation (effective reduction of μ) and consequently influences L_d, L_q and torque ripple behavior [12,19,21]. In this study, all voltage and current values are expressed as effective (RMS) values. The phase waveforms of the back-EMF are presented in terms of peak values in order to enable a clearer analysis of waveform symmetry and harmonic content. The primary reason for preferring peak values in back-EMF analysis is that harmonic distortions and waveform characteristics can be observed more distinctly compared to RMS values. The MQS assumption is considered valid within the low-frequency operating range of the investigated machines, where displacement current effects are negligible, and magnetic saturation is accounted for in the FEM simulations through nonlinear B–H material characteristics of the core materials.

3.1.2. Magnetic Vector Potential and Flux Distribution

In FEM-based solutions, the magnetic field is generally expressed using the magnetic vector potential A:

$$\mathrm{B} = \nabla \times \mathrm{A} \tag{5}$$

Here, A denotes the magnetic vector potential[29]. This quantity forms the direct physical basis of the magnetic flux distribution and magnetic flux density maps presented in this study. When the rotor flux barrier geometry is modified, the magnetic flux path through the rotor changes: this directly affects the saturation levels occurring in the stator teeth, rotor barrier tips, and bridge regions. Especially in hybrid barrier structures, the stronger suppression of q-axis leakage flux and the concentration of d-axis flux can be interpreted through the variations observed in the A and B distributions.

3.1.3. d-Axis Magnetic Model

In SynRMs, the d-axis represents the direction along which magnetic flux flows through a low-reluctance path. The fundamental harmonic stator surface current loading on the d-axis is defined as[30]:

$$\hat{K}_{sd} = \frac{3 k_w N_s \hat{I}_d}{\pi D_s} \tag{6}$$

Where k_w is the winding factor, N_s is the number of series conductors per phase, $\hat{I}_d$ is the fundamental amplitude of the d-axis current, and D_s is the stator inner diameter. In this study, k_w, N_s, and D_s are kept constant for all 34 motors. Therefore, variations in d-axis electrical loading mainly originate from indirect effects of rotor geometry, such as flux path modification and magnetic saturation. The d-axis scalar magnetic potential (Magnetomotive Force (MMF) equivalent) is given by:

$$\hat{U}_{sd} = \frac{\hat{K}_{sd} D_s}{2p} \tag{7}$$

where p denotes the number of pole pairs. The air-gap d-axis magnetic flux density is expressed as:

$$\hat{B}_{gd} = \frac{\mu_0 \hat{U}_{sd}}{g k_c k_{sat}} \tag{8}$$

Here, μ_0 is the permeability of free space, g is the air-gap length, k_c is the Carter coefficient accounting for slotting effects, and k_{sat} is the magnetic saturation coefficient. Changes in rotor barrier geometry and bridge dimensions alter the effective value of k_{sat}, particularly in regions of high flux density, thereby affecting the d-axis inductance L_d [12,21,29]. The d-axis flux linkage is finally given by:

$$\lambda_d = L_d i_d \tag{9}$$

where λ_d is the d-axis flux linkage, L_d is the d-axis inductance, and i_d is the d-axis current[31]. In this study, the primary objective of hybrid rotor structures is to increase the saliency ratio L_d/L_q by preserving the d-axis flux path while increasing the q-axis reluctance.

3.2. q-Axis Model and the Effect of Flux Barriers

3.2.1. q-Axis Electrical Loading

The q-axis corresponds to the high-reluctance direction imposed by the rotor flux barriers. The q-axis electrical loading is defined as[30]:

$$\hat{K}_{sq} = \frac{3 k_w N_s \hat{I}_q}{\pi D_s} \tag{10}$$

where $\hat{I}_q$ denotes the fundamental amplitude of the q-axis current. In this study, the i_d and i_q current components are determined according to a current angle strategy that maximizes torque production. Since the stator remains unchanged, variations in $\hat{K}_{sq}$ primarily reflect changes in q-axis flux linkage caused by rotor geometry.

3.2.2. Flux Barriers, Reluctance, and Saturation

Each flux barrier on the rotor introduces an additional reluctance to the q-axis magnetic circuit. The reluctance of the j-th barrier is given by:

$$R_{bj} = \frac{t_{bj}}{\mu_0 L_{stk} A_{bj}} \tag{11}$$

Where t_{bj} denotes the effective flux path length along the barrier, $A_{bj} = W_{bj} \cdot H_{bj}$ represents the effective cross-sectional area of the barrier, W_{bj} is the barrier width, H_{bj} is the barrier height, and L_{stk} denotes the stack length. In all analyzed designs, identical magnetic core materials are employed for the stator and rotor, ensuring that the observed performance variations originate solely from differences in rotor flux barrier geometry. In this study, the barrier width (W) and barrier height (H) are jointly defined as optimization variables. In this manner, the q-axis reluctance can be precisely controlled not only through the number of barriers but also via the geometric proportions of the barriers. This enables hybrid barrier structures to be optimized not only topologically but also geometrically. The q-axis flux linkage is expressed as:

$$\lambda_q = L_q i_q \tag{12}$$

where λ_q denotes the q-axis flux linkage, L_q is the q-axis inductance, and i_q is the q-axis current. As the number of barriers increases and hybrid geometries are employed, L_q generally decreases: this increases the saliency ratio L_d/L_q and enhances the reluctance torque. However, it has been emphasized that if saturation at the barrier tips and air-gap harmonics increase, torque ripple rises again: therefore, optimization becomes critical [21,24].

3.3. Torque, Power, and Harmonic Behavior

3.3.1. Electromagnetic Torque Production

In SynRMs, the electromagnetic torque can be expressed using the dq-axis model as:

$$T_e = \frac{3}{2}p(\lambda_d i_q - \lambda_q i_d) \tag{13}$$

where p is the number of pole pairs[31]. If the linear region is assumed, with $\lambda_d = L_d i_d$ and $\lambda_q = L_q i_q$, the torque expression becomes:

$$T_e = \frac{3}{2}p(L_d - L_q)i_d i_q \tag{14}$$

This expression clearly demonstrates why rotor flux barrier geometry is critical for torque production. The hybrid barrier structures proposed in this study aim to reduce L_q while preserving L_d as much as possible, thereby providing higher torque and an improved saliency ratio. The magnetic properties of the stator and rotor core materials are modeled using nonlinear B–H curves provided by the manufacturer datasheet. The same material is used for both stator and rotor cores in all designs to ensure a consistent comparison. The nonlinear magnetic saturation behavior is fully considered in the FEM simulations, allowing accurate representation of flux density distribution and saturation effects, particularly in rotor bridge regions and stator tooth tips.

3.3.2. Power Definitions and Losses

In this study, the mechanical output power is defined as:

$$P_{out} = T_{avg} \cdot \omega_m \tag{16}$$

$$\omega_m = 2\pi \cdot \frac{n}{60} \tag{17}$$

where P_{out} denotes the mechanical output power, T_{avg} the average electromagnetic torque, ω_m the mechanical angular speed, and n the mechanical speed. The electrical input power in this study is expressed as:

$$P_{in} = 3V_{rms}I_{rms}\cos\varphi \tag{18}$$

where P_{in} is the input power, V_{rms} the phase RMS voltage, I_{rms} the phase RMS current, and $\cos\varphi$ the power factor. The overall power balance is given by:

$$P_{in} = P_{out} + P_{loss} \tag{19}$$

and the total losses are modeled as:

$$P_{loss} = P_{cu} + P_{Fe} + P_{mech} \tag{20}$$

where P_{cu} represents the copper losses, P_{Fe} the iron losses, and P_{mech} the mechanical losses[32]. In this study, individual loss components are not modeled separately: instead, the total loss is evaluated indirectly based on the power balance by computing the mechanical output power from the average electromagnetic torque and speed, and subtracting it from the electrical input power. Since the same stator structure is used in all designs in this study, the trend of P_{cu} is largely similar: however, the rotor barrier geometry plays a more dominant role in P_{Fe} by affecting the flux density distribution and harmonics. Therefore, in hybrid geometries, a reduction in torque ripple may, in some cases, also lead to an improvement in iron losses due to reduced peak flux density levels.

3.3.3. Torque Ripple and Back-EMF Harmonics

Torque ripple is defined as:

$$TR(\%) = \frac{T_{max} - T_{min}}{T_{avg}} \times 100 \tag{21}$$

where TR denotes the torque ripple (%), T_{max} the maximum torque, T_{min} the minimum torque, and T_{avg} the average torque[32]. This metric is of critical importance, particularly for applications requiring quiet operation at low speeds (direct-drive systems, door actuators, etc.). Torque ripple is strongly associated with torque vibration and acoustic noise [19,24]. Back-EMF is analyzed as it directly reflects the spatial harmonic content introduced by the rotor flux-barrier geometry and provides a physically meaningful indicator of electromagnetic waveform distortion, which is closely linked to torque ripple and control quality in SynRMs. The back-EMF is given by:

$$e(t) = \frac{d\lambda(t)}{dt} \tag{22}$$

where $e(t)$ denotes the phase back-EMF, $\lambda(t)$ the time-varying flux linkage, and t the time. The Fourier expansion is expressed as:

$$e(t) = \sum_{h=1}^{\infty} E_h \sin(h\omega_e t + \varphi_h) \tag{23}$$

where E_h is the amplitude of the h-th harmonic, h the harmonic order, ω_e the electrical angular speed, and φ_h the harmonic phase angle. The Total Harmonic Distortion (THD) is defined as:

$$THD = \frac{\sqrt{\sum_{h=2}^{\infty} E_h^2}}{E_1} \tag{24}$$

In the THD calculation, harmonic components up to the 7th order are considered, as higher-order harmonics exhibit negligible amplitudes in the Fast Fourier Transform (FFT) spectra and have a limited impact on torque ripple and electromagnetic performance. This selection is further justified by the fact that, in low-speed OR-SynRM applications, lower-order harmonics dominate the electromagnetic torque pulsations and acoustic behavior, while higher-order components contribute marginally and can be reasonably neglected without loss of analytical accuracy. Within the scope of this study, the back-EMF waveform and FFT spectrum of four selected motors are analyzed to evaluate harmonic suppression behavior: it is shown that some hybrid barrier structures improve back-EMF quality by reducing low-order harmonics, thereby contributing to the reduction of torque ripple.

4. Materials and Methods

The optimization procedure begins with the systematic classification of rotor flux barrier geometries. As seen in Figure 1, four fundamental barrier types—elliptical, triangular, U1, and U2—are selected based on their widespread use in the literature. Using these geometries, both conventional dual-barrier (2B) and triple-barrier (3B) rotor structures, as well as their hybrid combinations, are developed. These geometries influence the magnetic flux distribution along the d- and q-axes, thereby affecting torque production, torque ripple, and back-EMF harmonic characteristics.

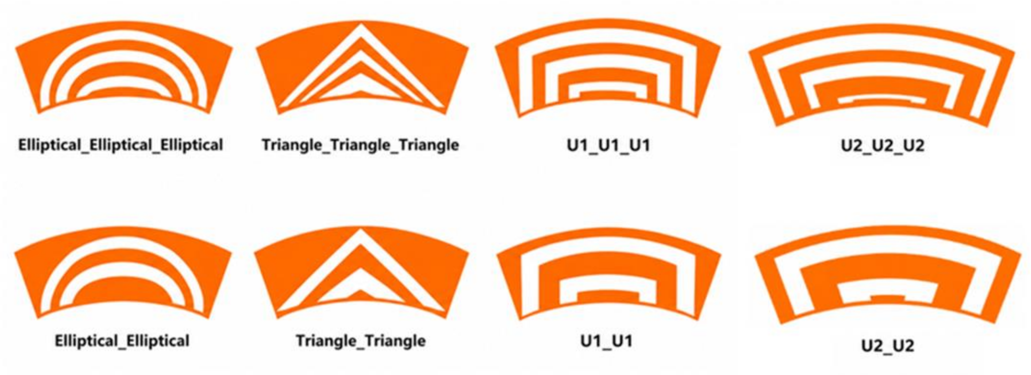

Figure 1. Cross-sectional comparison of the fundamental rotor flux barrier geometries (elliptical, triangular, U1, and U2) employed for two barrier (2B) and three barrier (3B) OR-SynRM designs.

4.1. Definition and Classification of Rotor Flux-Barrier Topologies

In all designs, the stator geometry, winding configuration, and operating conditions are kept constant, while only the number, geometry, and arrangement of rotor flux barriers are varied. This ensures a consistent and isolated evaluation of rotor geometry effects on electromagnetic performance. A total of 34 rotor configurations are examined, classified into dual-barrier (2B) and triple-barrier (3B) groups. Hybrid structures are formed by combining different fundamental barrier geometries, enabling increased q-axis reluctance while maintaining the d-axis flux path. The example classification shown in Figure 2 forms the basis for subsequent comparative analyses.

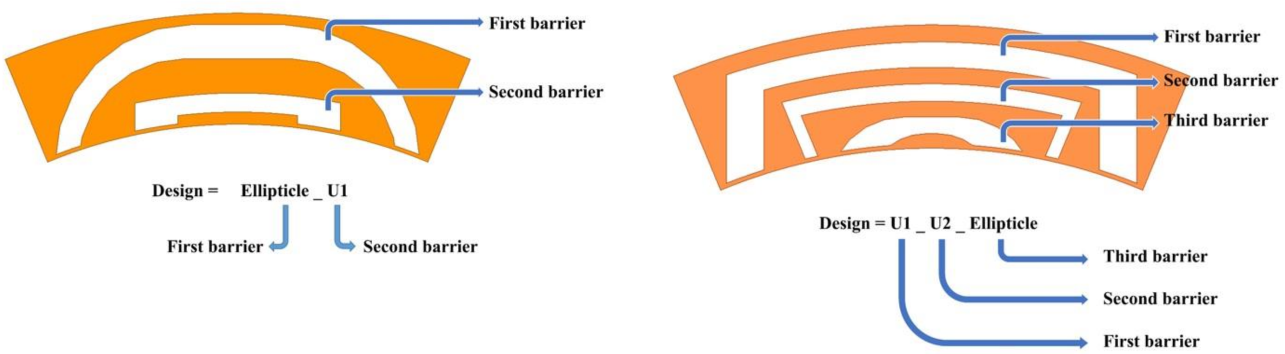

Figure 2. Schematic representation of hybrid rotor flux barrier topologies

4.2. Rotor Flux Barrier Parameterization and MOGA-Based Optimization Structure

For all rotor topologies investigated within the scope of this study, a common flux barrier parameterization approach and a MOGA-based optimization structure are applied in order to establish a comparable and consistent optimization framework. Although the total of 34 different rotor designs evaluated in the study differ in terms of the number of barriers (dual and triple barrier), barrier geometry (U1, U2, Elliptical, and Triangular), and barrier arrangement sequence, all designs are optimized using the same geometric parameter definitions and the same optimization strategy. Owing to this approach, the electromagnetic performances of different rotor configurations can be objectively compared within a common design space.

The optimization process in this study is conducted using the Multi-Objective Genetic Algorithm (MOGA) implemented in the Ansys Maxwell Optimetrics environment. Due to the internal structure of the software, explicit genetic parameters such as population size, number of generations, crossover rate, mutation rate, and selection method are automatically managed by the optimization engine and are not directly accessible or user-defined. Instead, the optimization process is characterized by the number of evaluated design variations and objective function definitions. In this study, approximately 1100 design variations were evaluated under predefined constraints. The stopping criterion is implicitly determined by the completion of the defined variation set and convergence toward stable objective values within the design space. Although an explicit convergence plot is not available, the consistency of the obtained results and the stability of the optimal solutions indicate a reliable convergence behavior of the optimization process. In addition, the optimization process reveals a trade-off between average torque and torque ripple, indicating that improvements in one objective may lead to compromises in the other. The distribution of the obtained solutions demonstrates that the proposed optimization framework effectively identifies balanced designs within the defined constraints. Furthermore, the consistency of the optimization results was verified through repeated evaluations, and similar solution trends were observed, confirming the stability and robustness of the MOGA-based optimization approach.

4.2.1. Rotor Flux-Barrier Parameterization Approach

As shown in Figure 3, the flow barriers common to the 34 motors are defined using effective radial thicknesses (hx, hy, hz) and tangential openings (Wx, Wy, Wz). Radial parameters influence d-axis flux continuity and saturation, whereas tangential parameters determine q-axis reluctance and flux leakage.

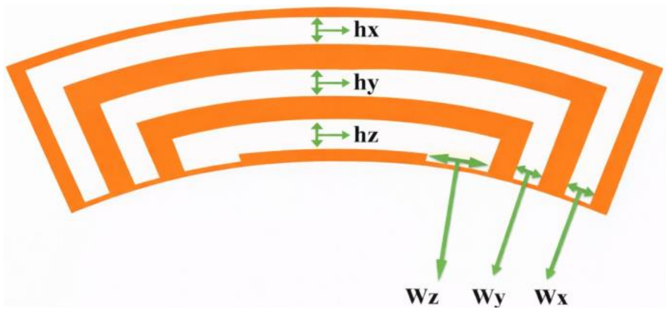

Figure 3. General MOGA optimization parameterization approach for the U2_U2_U2 rotor structure.

This representation enables different geometries to be evaluated within a common optimization structure. The optimization is formulated as a multi-objective problem, targeting average torque and torque ripple with equal weighting (50%–50%). Design constraints are defined as average torque ≥ 6 Nm and torque ripple ≤ 10%, ensuring suitability for low-speed, high-torque applications. The MOGA algorithm identifies Pareto-optimal solutions within this constrained design space.

4.2.2. General Evaluation of MOGA Optimization Results (Dual- and Triple-Barrier Rotors)

The MOGA optimization results obtained for dual-barrier rotor designs are presented in Table 1. As observed from Table 1, particularly for the basic rotor topologies U1_U1 and U2_U2, significant reductions in torque ripple are achieved together with torque enhancement after optimization. In hybrid rotor structures, the most dominant effect of MOGA is observed in suppressing torque ripple in configurations with high initial torque ripple. This indicates that the q-axis reluctance is effectively increased through the redistribution of tangential barrier openings by MOGA.

Table 1. MOGA-based optimization results for dual barrier rotors

Type	Design (barrier sequence)	Torque (Pre) [Nm]	Torque (Post) [Nm]	ΔTorque [%]	Torque ripple (Pre) [%]	Torque ripple (Post)[%]	ΔRipple [%]
Basic	Elliptical, Elliptical	7.29	6.88	-5.70	12.84	8.60	-33.00
Basic	Triangular, Triangular	4.92	5.20	+5.70	30.00	17.80	-40.70
Basic	U1, U1	7.10	7.30	+2.80	31.00	15.90	-48.70
Basic	U2, U2	6.68	7.40	+10.80	34.20	16.00	-53.20
Hybrid	Elliptical, Triangular	7.20	7.12	-1.00	47.00	38.50	-19.10
Hybrid	Elliptical, U1	7.17	7.3	+2.90	70.00	15.77	-77.50
Hybrid	Elliptical, U2	7.15	7.63	+6.70	52.72	51.36	-2.60
Hybrid	Triangular, Elliptical	4.51	2.24	-50.20	78.40	58.90	-24.90
Hybrid	Triangular, U1	3.44	5.41	+57.40	98.00	60.00	-38.80
Hybrid	Triangular, U2	3.25	2.10	-35.20	97.00	69.30	-28.60
Hybrid	U1, Elliptical	6.16	6.23	+1.10	86.00	55.00	-36.00
Hybrid	U1, Triangular	6.40	7.06	+10.40	82.00	60.20	-26.60
Hybrid	U1, U2	6.92	6.78	-2.00	91.00	29.00	-68.10
Hybrid	U2, Elliptical	6.35	6.78	+6.90	99.00	27.43	-72.30
Hybrid	U2, Triangular	6.75	5.99	-11.20	78.00	16.30	-79.10
Hybrid	U2, U1	6.29	6.32	+0.50	92.00	53.90	-41.40

The results for triple-barrier rotor designs are given in Table 2. In triple-barrier structures, a more balanced improvement in both torque enhancement and torque ripple control is observed compared to dual barrier designs. In particular, rotor configurations such as U2_U2_U2, U2_U1_Elliptical, and U2_Elliptical_Elliptical achieve average torque values approaching 8 Nm together with torque ripple reduced below 10% after optimization. These results demonstrate that with an increased number of barriers, MOGA can more effectively utilize the degrees of freedom in the design space. The relatively high torque ripple observed in some hybrid configurations can be attributed to localized magnetic saturation and asymmetric flux distribution in rotor barrier regions. These effects distort the air-gap flux waveform and increase harmonic components, leading to higher torque oscillations(See Table 1).

Table 2. MOGA-based optimization results for triple barrier rotors

Type	Design (barrier sequence)	Torque (Pre) [Nm]	Torque (Post) [Nm]	ΔTorque [%]	Torque ripple (Pre) [%]	Torque ripple (Post) [%]	ΔRipple [%]
Basic	Elliptical, Elliptical, Elliptical	7.90	7.99	+1.20	15.00	9.80	-34.70
Basic	Triangular, Triangular, Triangular	5.03	5.71	+13.50	24.00	16.80	-30.00
Basic	U1, U1, U1	7.76	7.95	+2.50	21.00	9.60	-54.30
Basic	U2, U2, U2	7.60	8.00	+5.30	17.30	8.10	-53.20
Hybrid	Elliptical, Elliptical, Triangular	7.80	7.47	-4.20	19.84	15.40	-22.40
Hybrid	Elliptical, Elliptical, U1	7.23	7.79	+7.70	32.40	20.86	-35.60
Hybrid	Elliptical, Elliptical, U2	7.55	7.89	+4.60	56.00	20.20	-63.90
Hybrid	U1, U1, Triangular	7.45	7.95	+6.80	37.00	15.17	-59.00
Hybrid	U1, Elliptical, Elliptical	7.86	7.53	-4.20	24.00	13.03	-45.70
Hybrid	U1, Elliptical, U1	7.23	7.77	+7.60	38.00	11.05	-70.90
Hybrid	U1, U1, Elliptical	7.87	7.51	-4.50	18.00	10.60	-41.10
Hybrid	U1, U2, Elliptical	6.99	7.61	+9.00	23.50	16.18	-31.10
Hybrid	U2, Elliptical, Triangular	7.30	7.65	+4.90	40.00	29.59	-26.00
Hybrid	U2, Elliptical, Elliptical	7.98	8.02	+0.60	18.70	9.55	-48.90
Hybrid	U2, Elliptical, U2	7.51	7.52	+0.20	43.00	18.80	-56.30
Hybrid	U2, U1, Elliptical	7.69	8.03	+4.50	59.00	8.10	-86.30
Hybrid	U2, U2, Elliptical	8.02	8.02	+0.00	14.20	7.90	-44.40
Hybrid	U2, U2, U1	7.96	7.97	+0.10	12.81	9.20	-28.20

4.2.3. Examination of the Geometric Influence of MOGA Using an Example Motor

In order to demonstrate the direct effect of MOGA-based optimization on rotor geometry, the U2_U2_U2 rotor design is considered as an example motor. The pre-optimization and post-optimization barrier parameters of this design are presented in Table 3. As seen in Table 3, as a result of the optimization process, the radial thicknesses of the first and second barriers (h_x, h_y) are increased, while the radial thickness of the third barrier (h_z) is reduced. This contributes to balancing magnetic saturation in the inner region of the rotor and to a more effective utilization of the d-axis flux path. Similarly, adjustments made to the tangential opening parameters (particularly the significant reduction in W_z) play a critical role in suppressing torque ripple by limiting flux leakage along the q-axis. It should be emphasized that Table 3 represents only a sample rotor configuration. The same parameterization approach and MOGA-based optimization structure are applied identically to all 34 rotor designs investigated in this study. As a result, by means of the developed common parameterization approach and MOGA-based optimization structure, rotor designs with different barrier geometries and arrangements are evaluated within a single design framework, and application-oriented balanced solutions between torque and torque ripple are obtained. The optimization results presented in this section provide a fundamental basis for the analyses of flux distribution, magnetic flux density, and electromagnetic torque characteristics detailed in the subsequent sections.

Table 3. U2_U2_U2 MOGA rotor barrier parameters (Pre-Opt / Post-Opt).

Parameter	Brief Description	Pre-Opt. (mm)	Post-Opt. (mm)
hx	Radial thickness of Barrier-1	5.00	6.84
hy	Radial thickness of Barrier-2	5.00	5.95
hz	Radial thickness of Barrier-3	5.00	3.04
Wx	Tangential opening of Barrier-1	5.00	5.91
Wy	Tangential opening of Barrier-2	5.00	6.20
Wz	Tangential opening of Barrier-3	12.00	7.64

5. Electromagnetic Performance Analysis of the Selected Best Designs

In this section, rotor designs developed for electromechanical drive applications operating at low speeds, providing sufficient output performance at relatively low power levels, and for which minimizing torque ripple during high-torque production is critical, are evaluated. Such operating conditions are commonly encountered in systems based on the direct-drive principle (e.g., linear sliding doors, etc.), in mechanisms requiring slow and controlled motion, and in applications with high sensitivity to vibration and noise. Within this scope, dual-barrier (2B) and triple-barrier (3B) rotor topologies are presented in separate tables: each design is compared in terms of the produced electromagnetic torque, torque ripple, power factor, efficiency, and the L_d/L_q ratio (λ). By considering basic and hybrid barrier arrangements together, the effects of hybridization on electromagnetic performance are clearly revealed. This general evaluation provides a basis for the detailed 2B and 3B comparisons to be performed in the subsequent subsections. In Table 4, the basic and hybrid variants of dual-barrier (2B) rotor topologies are compared. In particular, the balance between torque production capability and torque ripple in the low-speed region, and the effects of hybrid barrier configurations on power factor and efficiency, are examined.

Table 4. Electromagnetic Performance Results of Dual Barrier Rotor Designs

Category	Design (Barrier Sequence)	Torque (Nm)	Power Factor (–)	Torque Ripple (%)	Efficiency (%)	λ (Ld/Lq)
Basic	Elliptical_Elliptical	6.88	0.601	8.60	80.77	1.48
Basic	U1_U1	7.30	0.67	15.90	81.81	1.13
Basic	U2_U2	7.40	0.66	16.00	85.28	1.11
Basic	Triangular_Triangular	5.20	0.46	17.80	83.96	1.10
Hybrid	Elliptical_U1	7.38	0.67	15.77	85.33	1.12
Hybrid	U2_Triangular	5.99	0.54	16.30	79.07	1.11
Hybrid	U2_Elliptical	6.78	0.63	27.43	75.33	1.11
Hybrid	U1_U2	6.78	0.61	29.00	85.45	1.12
Hybrid	Elliptical_Triangular	7.12	0.65	38.50	83.48	1.12
Hybrid	Elliptical_U2	7.63	0.65	51.36	84.14	1.12
Hybrid	U2_U1	6.32	0.61	53.90	77.12	1.12
Hybrid	U1_Elliptical	6.23	0.61	55.00	77.29	1.13
Hybrid	Triangular_Elliptical	2.24	0.24	58.90	72.34	1.03
Hybrid	Triangular_U1	5.41	0.55	60.00	77.76	1.11
Hybrid	U1_Triangular	7.06	0.64	60.20	84.53	1.12
Hybrid	Triangular_U2	2.10	0.23	69.30	56.27	1.03

When Tables 4 and 5 are evaluated together, although it is known that an increase in the L_d/L_q ratio generally contributes positively to electromagnetic torque production, the obtained results indicate that this parameter does not determine motor performance alone. In some designs, the torque increase is significantly influenced by additional electromagnetic effects such as magnetic saturation, flux leakage, and the local flux density distribution within the rotor flux barriers. Therefore, a higher L_d/L_q ratio does not always imply a proportional improvement in efficiency or torque ripple: this reveals the necessity of addressing motor performance through a holistic electromagnetic evaluation. Table 5 presents the triple barrier (3B) rotor topologies. It is observed that triple barrier structures can suppress torque ripple more effectively, particularly in low-speed applications requiring high torque, and exhibit a more balanced behavior in power factor. In Table 6, among the dual and triple barrier designs, four representative designs that provide high torque production, low torque ripple, and an acceptable power factor–efficiency balance are selected. These designs clearly reflect the performance potential of basic and hybrid structures at different barrier counts. The superior performance of hybrid rotor flux barrier structures stems from the fact that these designs can provide a more balanced electromagnetic distribution between flux-guiding capability and magnetic saturation behavior compared to conventional single-geometry barrier structures.

Table 5. Electromagnetic Performance Results of Triple Barrier Rotor Designs

Category	Design (Barrier Sequence)	Torque (Nm)	Power Factor (–)	Torque Ripple (%)	Efficiency (%)	λ (Ld/Lq)
Basic	U2_U2_U2	8.00	0.67	8.10	83.10	1.13
Basic	U1_U1_U1	7.95	0.73	9.60	83.01	1.13
Basic	Elliptical_Elliptical_Elliptical	7.99	0.69	9.80	83.11	1.15
Basic	Triangular_Triangular_Triangular	5.71	0.53	16.80	82.88	1.36
Hybrid	U2_U2_Elliptical	8.02	0.69	7.90	82.49	1.13
Hybrid	U2_U1_Elliptical	8.03	0.70	8.10	82.50	1.13
Hybrid	U2_U2_U1	7.97	0.71	9.20	82.75	1.14
Hybrid	U2_Elliptical_Elliptical	8.02	0.70	9.55	83.55	1.14
Hybrid	U1_U1_Elliptical	7.51	0.65	10.60	87.35	1.12
Hybrid	U1_Elliptical_U1	7.77	0.67	11.05	83.40	1.13
Hybrid	U1_Elliptical_Elliptical	7.53	0.64	13.03	86.73	1.12
Hybrid	U1_U1_U2	7.95	0.72	15.17	85.89	1.13
Hybrid	Elliptical_Elliptical_Triangular	7.47	0.65	15.40	86.19	1.03
Hybrid	U1_U2_Elliptical	7.61	0.66	16.18	82.26	1.12
Hybrid	U2_Elliptical_U2	7.52	0.67	18.80	88.20	1.13
Hybrid	Elliptical_Elliptical_U2	7.89	0.68	20.20	84.93	1.13
Hybrid	Elliptical_Elliptical_U1	7.79	0.73	20.86	85.20	1.13
Hybrid	U2_Elliptical_Triangular	7.65	0.65	29.59	82.01	1.12

Table 6. Comparison of the selected four best rotor designs.

Category	Design (Barrier Sequence)	Torque (Nm)	Torque Ripple (%)	Efficiency (%)	Power Factor (–)	λ (Ld/Lq)
Basic 2B	Elliptical_Elliptical	6.88	8.60	80.77	0.60	1.48
Hybrid 2B	Elliptical_U1	7.38	15.77	85.33	0.67	1.12
Basic 3B	U2_U2_U2	8.00	8.10	83.10	0.67	1.13
Hybrid 3B	U2_U2_Elliptical	8.02	7.90	82.49	0.69	1.13

5.1. Comparative Analysis of Dual Barrier (2B) Rotor Designs

In this section, the electromagnetic performance of dual barrier (2B) rotor topologies is examined in detail. 2B designs constitute an important alternative for applications operating at low speeds and requiring sufficient torque production at relatively low power levels due to their structural simplicity and ease of manufacturing. However, in such applications, limiting torque ripple is a critical requirement for reducing vibration and acoustic noise. Within this scope, the basic elliptical barrier structure (Elliptical_Elliptical) and the hybrid barrier structure (Elliptical_U1) are comparatively addressed: evaluations are performed based on magnetic flux distribution, magnetic flux density, electromagnetic torque characteristics, and induced phase voltage waveforms. The comparisons are based on time-dependent FEM results obtained under the same operating conditions.

5.1.1. Magnetic Flux Distribution

The magnetic flux line distribution of the dual-barrier rotor designs is presented in Figure 4 (left) and Figure 4 (right). In the basic elliptical barrier design, it is observed that the magnetic flux is distributed in a similar manner along the rotor–stator air gap, and flux concentrations occur particularly at barrier tips and stator tooth roots. This indicates that the magnetic flux along the q-axis cannot be sufficiently suppressed and local saturation tendencies emerge in the magnetic circuit. In contrast, in the hybrid Elliptical_U1 design, due to the reshaping of the barrier geometry, it is observed that the magnetic flux follows a controlled path along the d-axis, although not with a large difference, and the q-axis flux is more effectively limited. The more symmetric and smooth distribution of flux lines contributes to a more stable operation of the reluctance torque mechanism. This improvement provides a significant advantage, particularly in terms of reducing torque ripple at low speeds.

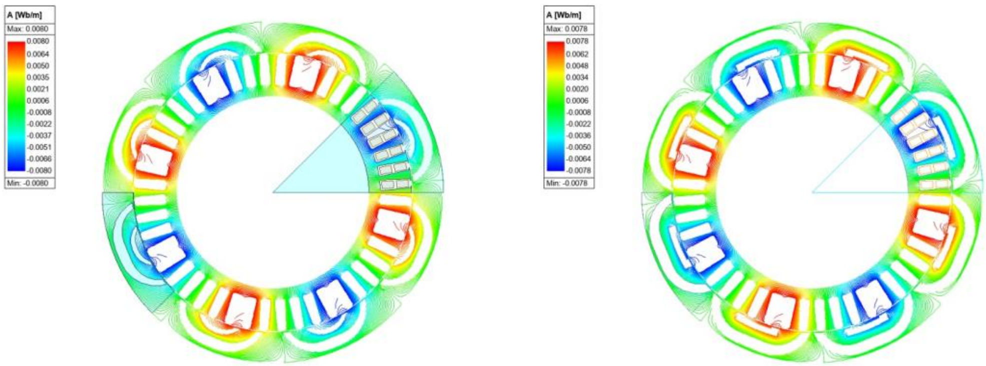

Figure 4. Magnetic flux-line distribution of 2B rotor designs – Elliptical_Elliptical and Elliptical_U1.

5.1.2. Magnetic Flux Density Distribution

The magnetic flux density distributions of the dual barrier rotor designs are given in Figure 5 (left) and Figure 5 (right). In the basic 2B elliptical design, it is observed that high magnetic flux density levels approaching 2000 mT occur locally at stator tooth tips and rotor barrier bridge regions. These regions are considered as critical areas where the risk of magnetic saturation increases. In the hybrid Elliptical_U1 design, it is noteworthy that the flux density distribution becomes more homogeneous and high B values are spread over a wider area. This indicates that local saturation regions are reduced and the magnetic circuit is utilized more effectively. This balancing in flux density contributes to a more uniform distribution of electromagnetic forces and indirectly helps reduce torque ripple. The differences in magnetic flux density distribution between the examined designs are primarily associated with the geometry of the rotor flux barriers. In conventional structures, flux tends to concentrate in narrow regions such as barrier tips and stator tooth edges, leading to localized magnetic saturation. In contrast, hybrid barrier configurations allow a more distributed flux path, reducing peak flux density levels and improving magnetic utilization. This more homogeneous distribution contributes to smoother electromagnetic force production and indirectly reduces torque ripple.

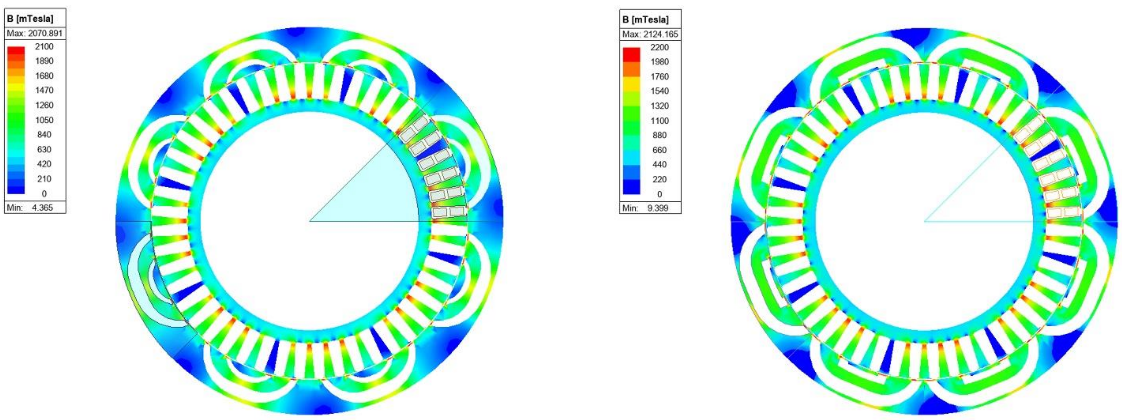

Figure 5. Magnetic flux-density distributions of 2B rotor designs: Elliptical_Elliptical (left) and Elliptical_U1 (right) [B, mT].

5.1.3. Electromagnetic Torque Characteristics

The time dependent electromagnetic torque waveforms of the dual barrier rotor designs are comparatively presented in Figure 6. The basic Elliptical_Elliptical design produces an average torque of 6.89 Nm while exhibiting pronounced yet relatively regular periodic oscillations in the torque waveform, originating from rotor–stator magnetic interactions and resulting in torque ripple. In the hybrid *Elliptical_U1* design, the average torque increases to 7.37 Nm: however, the torque waveform exhibits oscillations with higher amplitude and increased irregularity. Although the hybrid barrier geometry strengthens the reluctance torque component by more effectively suppressing the q-axis flux, this improvement introduces a clear trade-off between increased average torque and elevated torque ripple. Therefore, for low-speed direct-drive applications where vibration and acoustic sensitivity are critical, an increase in average torque alone should not be considered a sufficient indicator of superior electromagnetic performance.

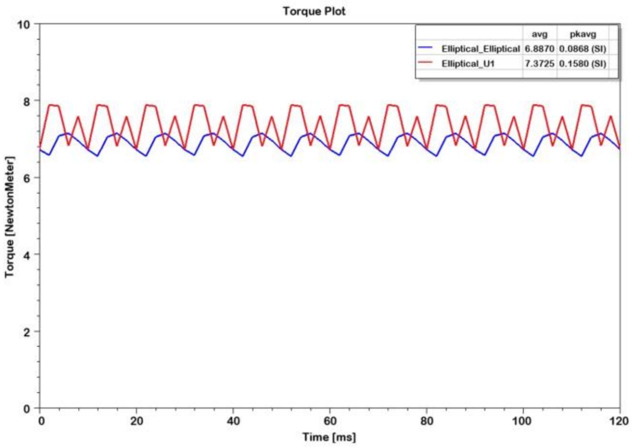

Figure 6. Electromagnetic torque waveforms of 2B rotor designs – Elliptical_Elliptical and Elliptical_U1.

The observed differences in torque characteristics between the basic and hybrid rotor structures can be explained by the interaction between flux distribution and magnetic saturation. In hybrid barrier geometries, the q-axis flux is more effectively suppressed, leading to an increased saliency ratio and consequently higher reluctance torque. However, the irregular distribution of magnetic flux at barrier tips and bridge regions introduces localized saturation effects. These localized saturation regions distort the air-gap flux density waveform, which results in increased torque ripple despite the improvement in average torque.

5.1.4. Induced Phase Voltage Waveforms

The induced phase voltage waveforms of the dual barrier rotor designs are given in Figure 7. In the basic elliptical design, the phase voltage waveform shows significant deviations from a sinusoidal form and contains high frequency harmonic components. This may cause additional filtering requirements on the drive side and current ripples. In the hybrid Elliptical_U1 design, it is noteworthy that the induced phase voltage waveform exhibits slightly more deviations and oscillations compared to the basic structure. The harmonic components provide a more unstable electromagnetic behavior in relatively low-speed and low power applications. These results can be interpreted such that, although the hybrid barrier geometry increases torque performance to some extent, it may adversely affect the electrical waveform quality.

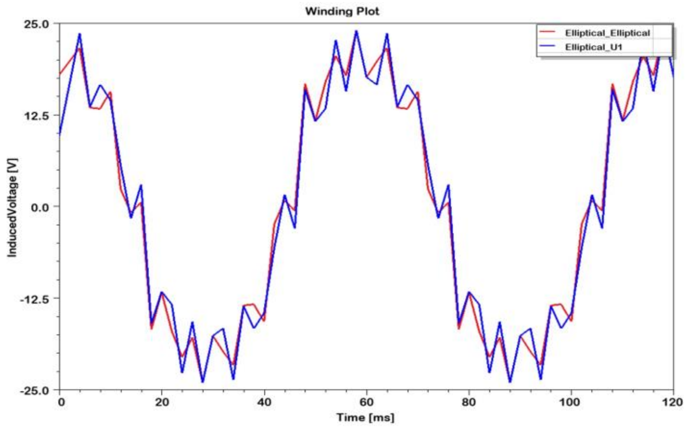

Figure 7. Induced phase voltage waveforms of 2B rotor designs.

5.2. Performance Evaluation of Triple-Barrier Rotor Designs

In this section, the electromagnetic performances of the best basic and best hybrid designs obtained in the triple barrier rotor class are comparatively evaluated. Within the scope of the investigation, the basic triple barrier U2_U2_U2 design and the hybrid triple-barrier U2_U2_Elliptical design are considered: analyses are conducted based on magnetic flux density, flux lines, electromagnetic torque characteristics, and induced phase voltage (back-EMF) waveforms. The comparisons are made particularly in terms of high torque production at low speeds and limiting torque ripple.

5.2.1. Magnetic Flux Distribution

The magnetic flux lines of the triple barrier designs are given in Figure 8. In the hybrid design, it is observed that the flux lines exhibit a slightly more regular and continuous structure along the d-axis compared to the basic barrier structure, although not with a large difference, and flux leakage in the q-axis direction is more effectively suppressed. This behavior confirms that the hybrid barrier arrangement improves the rotor saliency by enhancing the L_d/L_q ratio and enables a more effective production of reluctance torque. These results are also consistent with the trends obtained for the dual-barrier designs (see Section 5.1). The improved performance observed in triple-barrier rotor designs can be attributed to the increased number of degrees of freedom in shaping the magnetic flux paths. With additional barriers, the q-axis reluctance can be more effectively increased while preserving the continuity of the d-axis flux. This results in a more controlled flux distribution, reduced leakage flux, and a more stable electromagnetic torque production. Consequently, triple-barrier configurations provide a better balance between torque enhancement and torque ripple suppression.

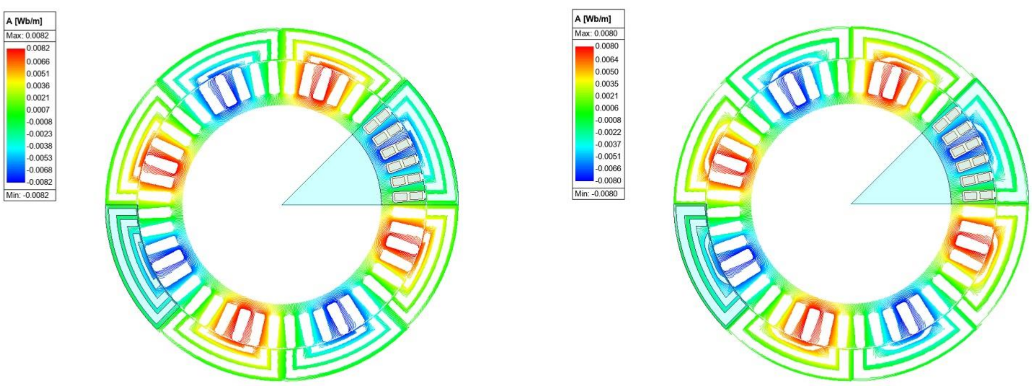

Figure 8. Comparison of magnetic flux lines for the best triple barrier rotor designs: basic U2_U2_U2 design (left) and hybrid U2_U2_Elliptical design (right).

5.2.2. Magnetic Flux Density Distribution

Figure 9 presents the magnetic flux density distributions of the basic and hybrid triple barrier designs. In the basic U2_U2_U2 structure, local saturation regions occur in rotor bridge regions and barrier tips, and the magnetic flux is concentrated in narrow cross sections.

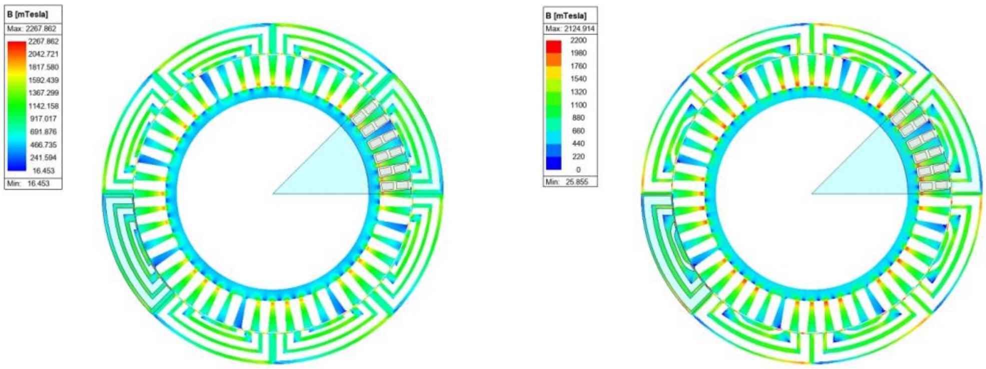

Figure 9. Comparison of magnetic flux density distributions for the best triple barrier rotor designs: basic U2_U2_U2 design (left) and hybrid U2_U2_Elliptical design (right)

In contrast, in the hybrid U2_U2_Elliptical design, due to the effect of the elliptical barrier geometry, it is observed that the flux transition paths are distributed more evenly and the maximum flux density regions are spread over a wider area. This indicates that the hybrid barrier approach improves the continuity of the magnetic circuit and is considered to reduce the saturation risk.

5.2.3. Electromagnetic Torque Characteristics

The electromagnetic torque waveforms are presented in Figure 10. Although both designs reach similar average torque levels, it is observed that torque ripple is significantly reduced in the hybrid U2_U2_Elliptical structure. This indicates that by using multiple barriers together with hybrid geometry, magnetic force oscillations are suppressed and a more stable torque production is achieved at low speeds. The obtained results are also consistent with the numerical torque ripple values given in Table 3.

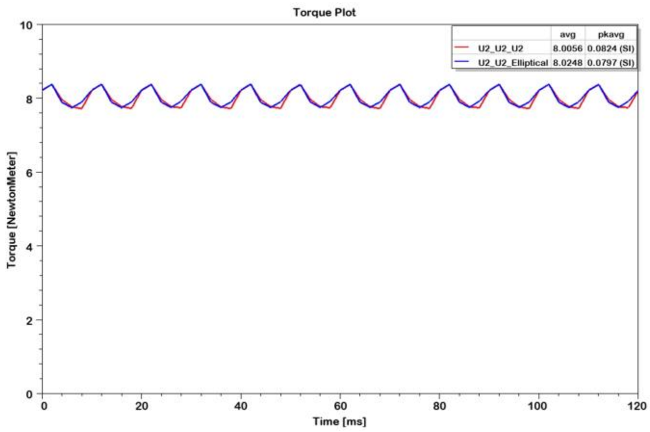

Figure 10. Comparison of electromagnetic torque waveforms for the best triple barrier rotor designs

5.2.4. Induced Phase Voltage Waveforms

Figure 11 compares the back-EMF waveforms of the triple barrier designs. In the hybrid design, it is observed that the waveform is closer to the fundamental sinusoidal component and higher order harmonics are relatively suppressed. This improvement contributes to both the reduction of torque ripple and the overall balancing of electromagnetic performance. This result indicates that the hybrid barrier geometry positively affects not only the static magnetic field distribution but also the dynamic electromagnetic behavior. Overall, it is concluded that in the triple barrier rotor class, the hybrid U2_U2_Elliptical design provides a more balanced and stable electromagnetic performance than the basic U2_U2_U2 design in terms of magnetic saturation distribution, flux-guiding effectiveness, suppression of torque ripple, and back-EMF harmonic content. These findings clearly demonstrate that in multi-barrier OR-SynRM designs, the hybrid barrier approach is an effective and applicable solution for low-speed–high-torque applications.

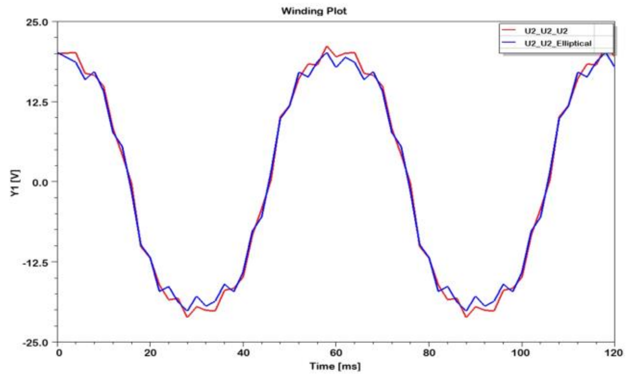

Figure 11. Comparison of induced phase voltage waveforms for the best triple barrier rotor designs

5.3. Back-EMF Harmonic Analysis and THD Comparison

In order to ensure a meaningful and focused harmonic analysis, only four representative motor designs are selected for FFT evaluation. These designs correspond to the best-performing configurations in each category, namely: the best basic and hybrid structures for both dual-barrier (2B) and triple-barrier (3B) rotor groups. The selection is based on a combined assessment of average torque, torque ripple, efficiency, and power factor, as presented in Table 6. By selecting the most representative designs from each category, the harmonic behavior can be evaluated in a clear and comparative manner without introducing unnecessary redundancy. Considering that all 34 designs exhibit similar fundamental electromagnetic behavior trends, analyzing all configurations in the frequency domain would not provide additional significant insight, but would reduce the clarity of the presented results. Therefore, the selected four designs effectively represent the overall behavior of the entire design space, allowing a clear interpretation of the influence of rotor topology on harmonic performance.

In this section, the phase back-EMF harmonic contents of the best four motor designs identified in the study are comparatively examined. The analyses are performed for the dual barrier basic structure (Elliptical_Elliptical), the dual barrier hybrid structure (Elliptical_U1), the triple barrier basic structure (U2_U2_U2), and the triple-barrier hybrid structure (U2_U2_Elliptical). When the raw FFT spectra presented in Figure 12 are examined, it is observed that the fundamental harmonic component (H1) is dominant in all motors. However, particularly for the dual barrier hybrid structure (Elliptical_U1), it is noteworthy that the amplitudes of the 3rd, 5th, and 7th harmonic components are higher compared to the other designs. This indicates that the effect of hybrid barrier geometry on the back-EMF waveform influences not only the fundamental component but also higher order harmonics significantly. Comparative results of THD and fundamental harmonic amplitudes are given in Figure 13. Therefore, the selected motor set is considered sufficient to represent the general harmonic characteristics of the investigated rotor topologies without requiring the analysis of all 34 designs. The variation in harmonic content observed among different rotor designs is directly related to the spatial distribution of magnetic flux and the resulting air-gap flux density waveform. Hybrid barrier structures may introduce additional spatial harmonics due to geometric asymmetries and localized saturation effects. While some configurations improve the fundamental component, others increase higher-order harmonics, leading to a trade-off between torque production and waveform quality. Therefore, minimizing torque ripple requires not only maximizing average torque but also ensuring a smooth and sinusoidal flux distribution in the air gap.

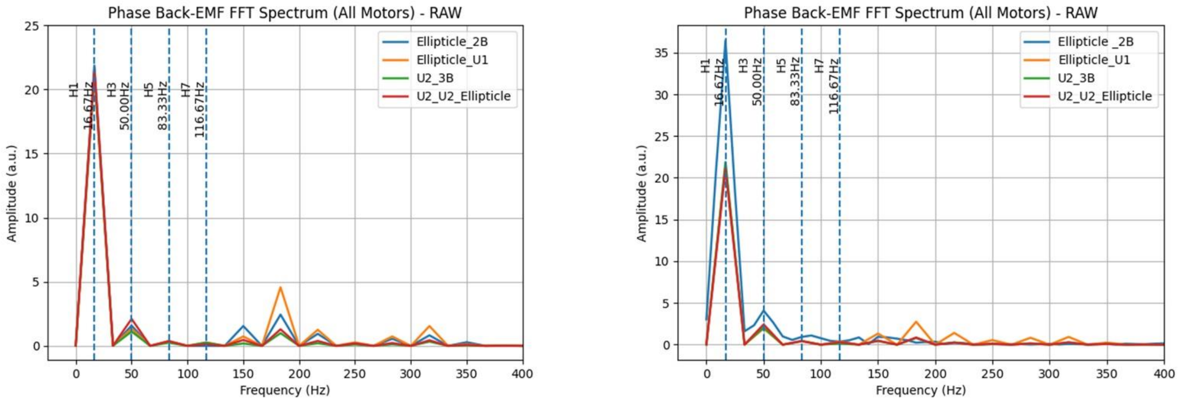

Figure 12. Raw FFT spectra of phase back-EMF for the four best motor designs.

The results reveal that the U2_U2_U2 design has the lowest THD value and provides the most balanced structure in terms of harmonics. In contrast, the increase in the THD value in the Elliptical_U1 design indicates that a trade-off occurs in terms of harmonic quality despite the torque increase. The hybrid triple barrier structure (U2_U2_Elliptical) exhibits a balanced performance in terms of both the fundamental harmonic amplitude and THD. The evaluation based on the back-EMF spectrum and THD not only indicates the quality of the waveform but also provides an indirect indicator regarding voltage quality and current ripple tendencies from the drive perspective. Indeed, in OR-SynRM designs, it has been demonstrated in previous studies through FEA and experimental investigations using the MOGA method that the geometry and positioning of rotor flux barriers directly affect the electromagnetic field distribution and, accordingly, torque ripple and harmonic contents, and that a smoother electromagnetic behavior can be achieved through optimization of rotor barriers[33].

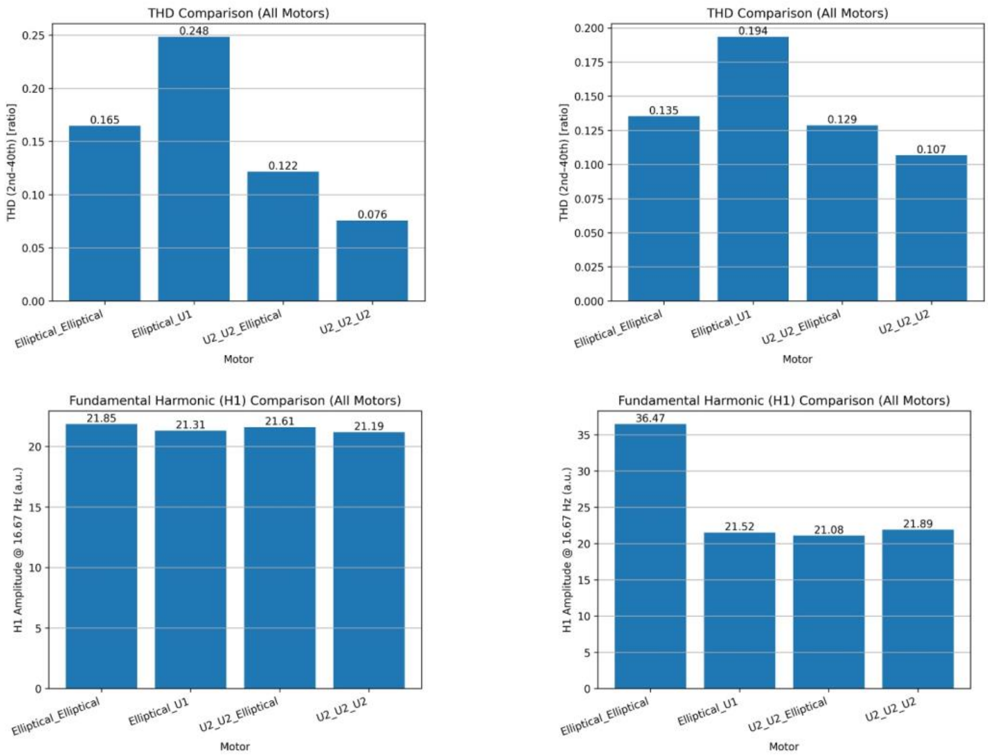

Figure 13. Comparison of fundamental back-EMF harmonic magnitude and THD for the four motors.

In addition, it is emphasized that the accuracy of back-EMF based modeling and observer/sensorless approaches in SynRMs is sensitive to machine parameters (especially saliency and rotor geometry): therefore, the effect of rotor geometry on electrical waveforms should also be examined [34]. The FFT spectra normalized such that the fundamental harmonic amplitude H1 = 1 are presented in Figure 14.

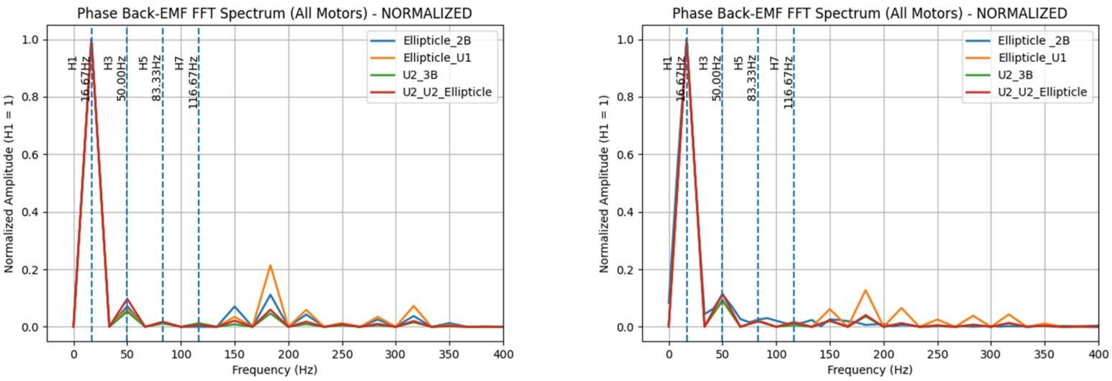

Figure 14. Normalized back-EMF FFT spectra for the four best motor designs.

This normalized comparison reveals the differences in harmonic distribution among the designs more clearly. In particular, it is clearly seen that higher-order harmonics are suppressed in triple-barrier designs, whereas harmonic concentrations occur at certain frequencies in the dual-barrier hybrid structure. The obtained results indicate that the rotor barrier number and barrier geometry are decisive not only for electromagnetic torque but also for back-EMF harmonic content and thus drive compatibility.

6. General Evaluation and Conclusions

In this study, the electromagnetic performance of OR-SynRMs is comprehensively investigated through the combined use of systematic variation of rotor flux barrier geometries, detailed electromagnetic analyses based on Maxwell's equations using the FEM, and a MOGA-based optimization approach. In all motor models, the stator geometry, winding structure, and operating conditions are kept constant: only the number, geometry, and arrangement sequence of the flux barriers on the rotor are varied, and a total of 34 different rotor configurations are evaluated. Through this methodology, it is clearly demonstrated that the observed performance differences originate directly from the rotor geometry. Based on four fundamental flux barrier geometries widely adopted in previous research (Elliptical, Triangular, U1, and U2), two- and three barrier basic designs and their hybrid combinations are evaluated using FEM-based time-stepping electromagnetic analyses and optimized using the MOGA algorithm. During the optimization process, the average electromagnetic torque and torque ripple are included as objective functions with equal weighting (50%–50%): additionally, engineering constraints of average torque ≥ 6 Nm and torque ripple ≤ 10% are imposed. In this way, rotor designs that not only produce high torque but also exhibit low vibration and acoustic noise potential are targeted.

The FEM results indicate that increasing the number of barriers, and particularly employing hybrid barrier geometries, enables more effective enhancement of q-axis reluctance while preserving the d-axis flux path. This directly contributes to improving the saliency ratio (L_d/L_q), increasing the average torque, and suppressing torque ripple. In three-barrier hybrid rotor structures, an average torque of approximately 8 Nm together with torque ripple below 10% is achieved: this performance exhibits a more balanced electromagnetic behavior compared to two-barrier designsComparative FEM analyses conducted on the selected four best rotor designs reveal that hybrid flux-barrier OR-SynRM structures can increase the average torque by 7.27% in the two-barrier group and by 0.33% in the three-barrier group compared to the basic designs: torque ripple is reduced by 2.47% only in the three-barrier hybrid structure, while the saliency ratio (L_d/L_q) generally shows limited variation. Back-EMF harmonic analyses further demonstrate that hybrid rotor topologies do not provide a unidirectional reduction in harmonic content:

in some hybrid configurations, the THD increases, whereas in suitable barrier combinations, the THD decreases, resulting in a more balanced spectral distribution. This indicates that the primary advantage of hybrid designs lies not merely in suppressing harmonic magnitudes but in rendering the electromagnetic behavior more balanced and controllable. This interpretation is also consistent with recent studies showing that magnetic material behavior, operating-point shifts on the B–H curve, and safe operating limits play a decisive role in maintaining stable electromagnetic performance under different loading conditions [35]. In conclusion, this study clearly demonstrates that in OR-SynRMs, rotor flux barrier geometry should be addressed not only in terms of barrier count but also through FEM supported hybridized geometric arrangements, which are critical for achieving a balanced trade-off among torque, torque ripple, and harmonic performance. The proposed FEM–MOGA based holistic optimization approach provides a robust and generalizable design framework for OR-SynRM design in direct-drive applications requiring high torque at low speed and exhibiting sensitivity to vibration and noise (particularly automatic linear sliding door systems). Similarly, recent motor design studies based on the combined use of analytical modeling and Ansys RMxprt/Maxwell simulations have demonstrated that systematic geometry refinement can yield measurable efficiency and performance improvements in practical electrical-machine applications [36].

In order to further evaluate the effectiveness of the proposed design approach, a direct comparison with representative studies in the literature is provided. For example, in the study presented in [15], an outer-rotor synchronous reluctance motor designed for scooter applications achieved an average torque level of approximately 6–7 Nm, with torque ripple values reported above 10% under comparable low-speed operating conditions. Similarly, in [16], although optimization improved the electromagnetic performance, torque ripple reduction remained limited due to the use of conventional rotor geometries.

In contrast, the results obtained in this study demonstrate that the proposed hybrid rotor flux-barrier configurations can achieve average torque values up to approximately 8 Nm while maintaining torque ripple levels below 10%, particularly in triple-barrier structures such as U2_U2_Elliptical. This comparison indicates that the hybridization of rotor flux barrier geometries, combined with a systematic MOGA-based optimization framework, provides a more effective balance between torque production and torque ripple suppression compared to conventional designs reported in the literature.

Despite the comprehensive evaluation presented in this study, several limitations should be acknowledged. First, the analysis is limited to electromagnetic performance based on two-dimensional FEM simulations, and mechanical effects such as rotor stress, vibration, and thermal behavior are not considered. These aspects may influence the practical applicability of the proposed designs and should be addressed in future studies. Second, although the MOGA-based optimization framework provides effective results, the optimization parameters are kept constant for all designs, and the influence of different optimization strategies is not investigated in detail. Finally, the results are not validated through experimental prototyping, and therefore, the findings should be interpreted within the context of simulation-based analysis. Future work will focus on extending the proposed design framework to include multi-physics analysis and experimental validation in order to further enhance the reliability and applicability of the results.

Declaration of Competing Interest

The authors of the article declare that they have no personal or financial conflicts of interest with any institution, organisation or individual.

References

[1] Lavrinovicha L, Dirba J, Dobriyan R. Design of low-torque-ripple synchronous reluctance motor with external rotor. Latvian Journal of Physics and Technical Sciences 2017;54(1):23–30. https://doi.org/10.1515/lpts-2017-0003

[2] Dirba J, Dobriyan R, Lavrinovicha L, Vitolina S. Comparison of synchronous reluctance motors with the outer and inner rotor. Latvian Journal of Physics and Technical Sciences 2017;54(3):25–36. https://doi.org/10.1515/lpts-2017-0017
[3] Lavrinovicha L, Dobriyan R, Onzevs O. Metamodels for optimum design of outer-rotor synchronous reluctance motor. Electrical, Control and Communication Engineering 2014;5(1):34–39. https://doi.org/10.2478/ecce-2014-0005
[4] Inte RA, Jurca FN. A novel synchronous reluctance motor with outer rotor for an electric bike. In: International Conference and Exposition on Electrical and Power Engineering; 2016; Iasi, Romania. 213–218. https://doi.org/10.1109/ICEPE.2016.7781335
[5] Inte RA, Jurca FN, Martis C. A study of the rotor design influence in power factor value of ORSynRM. In: 12th International Conference on ELEKTRO; 2018; Mikulov, Czech Republic. 1–6. https://doi.org/10.1109/ELEKTRO.2018.8398287
[6] Jurca FN, Martis C. Analysis of outer rotor synchronous reluctance motor for low-speed applications. In: 19th International Conference on Electrical Drives and Power Electronics; 2017; Dubrovnik, Croatia. 242–247. https://doi.org/10.1109/EDPE.2017.8123239
[7] Islam MZ, Choi S, Elbuluk ME, Bonthu SSR, Arafat A, Baek J. Design of external rotor ferrite-assisted synchronous reluctance motor for high power density. Applied Sciences 2021;11(7):3102. https://doi.org/10.3390/app11073102
[8] Deshpande Y, Toliyat HA. Design of an outer rotor ferrite assisted synchronous reluctance machine for electric two-wheeler application. In: IEEE Energy Conversion Congress and Exposition; 2014; Pittsburgh, PA, USA. 3147–3154. https://doi.org/10.1109/ECCE.2014.6953828
[9] Roohi Sankestani MM, Siadatan A. Design of outer rotor synchronous reluctance motor for scooter application. In: 10th International Power Electronics, Drive Systems and Technologies Conference; 2019; Shiraz, Iran. 393–398. https://doi.org/10.1109/PEDSTC.2019.8697885
[10] Khan MA, Khan F, Jamshed U, Ali S, Ajmal Z, Zahid A, Ahmad N. Design and analysis of outer segmental rotor synchronous reluctance machine for future electric bike. In: International Conference on Engineering and Emerging Technologies; 2019; Lahore, Pakistan. 1–5. https://doi.org/10.1109/CEET1.2019.8711839
[11] Raj MA, Kavitha A. Effect of rotor geometry on peak and average torque of external-rotor synchronous reluctance motor in comparison with switched reluctance motor for low-speed direct-drive domestic application. IEEE Transactions on Magnetics 2017;53(11):1–8. https://doi.org/10.1109/TMAG.2017.2710191
[12] Jurca NF, Inte RA, Popa DC, Varaticeanu B, Minciunescu P, Martis C. Electromagnetic and mechanical analysis of a modular outer rotor synchronous reluctance machine for light propulsion vehicles. IEEE Transactions on Transportation Electrification 2021;7(4):2798–2811. https://doi.org/10.1109/TTE.2021.3067135
[13] Bonthu SSR, Tarek MTB, Arafat AKM, Islam MZ, Choi S. Fault-tolerant performance comparisons between external and internal rotor PMa-SynRMs. In: IEEE Applied Power Electronics Conference and Exposition; 2018; San Antonio, TX, USA. 2933–2939. https://doi.org/10.1109/APEC.2018.8341436
[14] Bonthu SSR, Islam MZ, Arafat AKM, Choi S. Five-phase external rotor permanent magnet assisted synchronous reluctance motor for in-wheel applications. In: IEEE Transportation Electrification Conference and Expo; 2017; Chicago, IL, USA. 586–591. https://doi.org/10.1109/ITEC.2017.7993336
[15] Salehinia SR, Afjei E, Hekmati A, Aghazadeh H. Design procedure of an outer rotor synchronous reluctance machine for scooter application. International Journal of Engineering 2021;34(3):656–666. https://doi.org/10.5829/IJE.2021.34.03C.10
[16] Jurca FN, Inte RA, Martis C. Optimal rotor design of novel outer rotor reluctance synchronous machine. Electrical Engineering 2020;102(1):107–116. https://doi.org/10.1007/s00202-019-00786-w
[17] Moradi CheshmehBeigi H, Behroozi L. Analytical design, electromagnetic field analysis and parametric sensitivity analysis of an external rotor permanent magnet-assisted synchronous reluctance motor. Electrical Engineering 2020;102(4):1947–1957. https://doi.org/10.1007/s00202-020-01006-6
[18] Al-Ani M. Multi-physics design and analyses of dual rotor synchronous reluctance machine. eTransportation 2021;8:100113. https://doi.org/10.1016/j.etran.2021.100113
[19] Bonthu SSR, Tarek MTB, Choi S. Optimal torque ripple reduction technique for outer rotor PM synchronous reluctance motor. IEEE Transactions on Energy Conversion 2018;33(3):1315–1324. https://doi.org/10.1109/TEC.2017.2781259
[20] Bonthu SSR, Tarek MTB, Islam MZ, Choi S. Performance analysis of rare-earth and rare-earth-free external rotor motors under eccentricity faults. In: IEEE Applied Power Electronics Conference and Exposition; 2018; San Antonio, TX, USA. 2940–2946. https://doi.org/10.1109/APEC.2018.8341437

[21] Hefaz H, Afjei E, Ardestani M. Sensitivity analysis of rotor geometry for external-rotor synchronous reluctance motor using finite element method. In: 10th International Power Electronics, Drive Systems and Technologies Conference; 2019; Shiraz, Iran. https://doi.org/10.1109/PEDSTC.2019.8697807
[22] Dirba J, Lavrinovicha L, Dobriyan R. Study of the synchronous reluctance motor design. Latvian Journal of Physics and Technical Sciences 2016;53(4):22–29. https://doi.org/10.1515/lpts-2016-0025
[23] Mukherjee V, Sokolov M, Pippuri-Mäkeläinen J, Hinkkanen M, Belahcen A. Comparative study of inner and outer rotor bearingless synchronous reluctance motors. The Journal of Engineering 2019;2019(17):4375–4379. https://doi.org/10.1049/joe.2018.8195
[24] Inte RA, Jurca FN. Torque ripple reduction of outer rotor synchronous reluctance machine with concentrated winding. In: 19th International Conference on Electrical Drives and Power Electronics; 2017; Dubrovnik, Croatia. 248–252. https://doi.org/10.1109/EDPE.2017.8123240
[25] Aghazadeh H, Afjei SE, Siadatan A. Sensitivity analysis of external-rotor permanent magnet assisted synchronous reluctance motor. World Academy of Science, Engineering and Technology, International Journal of Energy and Power Engineering 2018;12(6):426–430. https://doi.org/10.5281/zenodo.1317186
[26] Inte RA, Jurca FN, Martis C. Analysis performances of outer rotor synchronous reluctance machine with or without permanent magnets for small electric propulsion application. In: 11th International Symposium on Advanced Topics in Electrical Engineering; 2019; Bucharest, Romania. 1–6. https://doi.org/10.1109/ATEE.2019.8724868
[27] Jin JM. The finite element method in electromagnetics. 3rd ed. Hoboken, NJ: Wiley; 2014.
[28] Bossavit A. Computational electromagnetism: variational formulations, complementarity, edge elements. Boston: Academic Press; 1998.
[29] Boldea I, Tutelea L. Reluctance electric machines: design and control. Boca Raton: CRC Press; 2019.
[30] Boldea I. Reluctance synchronous machines and drives. Oxford: Clarendon Press; 1996.
[31] Miller TJE. Brushless permanent-magnet and reluctance motor drives. Oxford: Clarendon Press; 1989.
[32] Pellegrino G, Vagati A, Guglielmi P, Boazzo B. Performance comparison between surface-mounted and interior PM motor drives for electric vehicle application. IEEE Transactions on Industrial Electronics 2012;59(2):803–811. https://doi.org/10.1109/TIE.2011.2151825
[33] Eser E, Üstkoyuncu N. Design and analysis of a novel axial flux permanent magnet assisted synchronous reluctance motor. Journal of Electrical Engineering and Technology 2025;20(3):1429–1438. https://doi.org/10.1007/s42835-024-02052-x
[34] Azhagar RM, Kavitha A. Effect of rotor geometry on peak and average torque of direct drive external-rotor synchronous reluctance motor (Ex-R SynRM) in comparison with switched reluctance motor for low speed domestic application. In: IEEE International Magnetics Conference (INTERMAG); 2017; Dublin, Ireland. 1–2. https://doi.org/10.1109/INTMAG.2017.8007641
[35] Yucel E, Cunkas M, Knypiński Ł. Evaluation of magnet demagnetization behavior in permanent magnet linear synchronous motors. Electrical Engineering and Energy 2025;4(1):52–63. https://doi.org/10.64470/elene.2025.1005
[36] Mutluer M. Improving performance of squirrel cage induction motor used in submersible pumps. Electrical Engineering and Energy 2025;4(2):28–35. https://doi.org/10.64470/elene.2025.1008